Applied-force oscillations in avalanche dynamics

Louis W. McFaul IV [1], Gregory Sparks [2], Jordan Sickle [1], Jonathan T. Uhl,[*] Wendelin J. Wright [3,4]
Robert Maaß [2], and Karin A. Dahmen[1,†]

[1]*Department of Physics and Institute of Condensed Matter Theory, University of Illinois at Urbana Champaign,*
1110 West Green Street, Urbana, Illinois 61801, USA

[2]*Department of Materials Science and Engineering and Frederick Seitz Materials Research Laboratory,*
University of Illinois at Urbana Champaign, Urbana, Illinois 61801, USA

[3]*Department of Mechanical Engineering, One Dent Drive, Bucknell University, Lewisburg, Pennsylvania 17837, USA*

[4]*Department of Chemical Engineering, One Dent Drive, Bucknell University, Lewisburg, Pennsylvania 17837, USA*

Until now most studies of discrete plasticity have focused on systems that are assumed to be driven by a monotonically increasing force; in many real systems, however, the driving force includes damped oscillations or oscillations induced by the propagation of discrete events or "slip avalanches." In both cases, these oscillations may obscure the true dynamics. Here we effectively consider both cases by investigating the effects of damped oscillations in the external driving force on avalanche dynamics. We compare model simulations of slip avalanches under mean-field dynamics with observations in slip-avalanche experiments on slowly compressed micrometer-sized Au specimens using open-loop force control. The studies show very good agreement between simulations and experiments. We find that an oscillatory external driving force changes the average avalanche shapes only for avalanches with durations close to the period of oscillation of the external force. This effect on the avalanche shapes can be addressed in experiments by choosing suitable specimen dimensions so that the mechanical resonance does not interact with the avalanche dynamics. These results are important for the interpretation of avalanche experiments with built-in oscillators, and for the prediction and analysis of avalanche dynamics in systems with resonant vibrations.

I. INTRODUCTION

Slip avalanches in slowly deformed solid materials have been studied in a variety of systems, ranging from slowly compressed nanocrystals to earthquakes [1–6]. These slip avalanches are often measured via acoustic emission pulses or as sudden stress drops or strain jumps in stress-strain curves [7–9]. In most previous studies of avalanche dynamics, the driving force is applied at the boundaries and increases linearly with time. Avalanches are triggered by this slow, quasistatic stress increase. However, if the applied force has an oscillatory component, these oscillations may interact with the avalanche dynamics [10,11]. For example, seismic waves passing through a fault system may induce oscillations in the applied stress on the seismic fault, and these oscillations can trigger earthquakes [12,13]. Indeed, oscillations in the applied force may be the norm rather than the exception in real-world avalanching systems. In this paper we report the effects that

applied-force oscillations have on experimental avalanches, and we compare the experimental shapes to simulated shapes using a recently developed model [10,11].

Avalanches often have a broad size distribution. Mean-field modeling and simulations suggest that the associated power-law statistics reflect an underlying nonequilibrium critical point [14,15]. The scaling behavior near this critical point is not affected by the microscopic details of the material, and therefore a mean-field model is able to predict some of the observed statistics and dynamics of experimental avalanches [16–20]. Renormalization group calculations show that approximating the physical interactions with mean-field elastic interactions (that do not decay with distance) gives the correct scaling behavior of the avalanche statistics on length scales that are large compared to the microscopic details [14,15]. In the model, the driving force is applied via a "boundary spring" that couples each region in the material to a boundary wall that moves at a slow constant velocity; the resulting increasing applied force transmitted by the boundary spring can then trigger avalanches [21,22].

We noted at the outset that the goal of this paper is to show how avalanche dynamics can be influenced by oscillations in the driving force. Our findings are meant to enable proper design of future experiments to avoid these issues. Here we use a mean-field model to illustrate our points, but our key result that oscillations may interact with avalanche dynamics depending on the relative timescales of each is

---
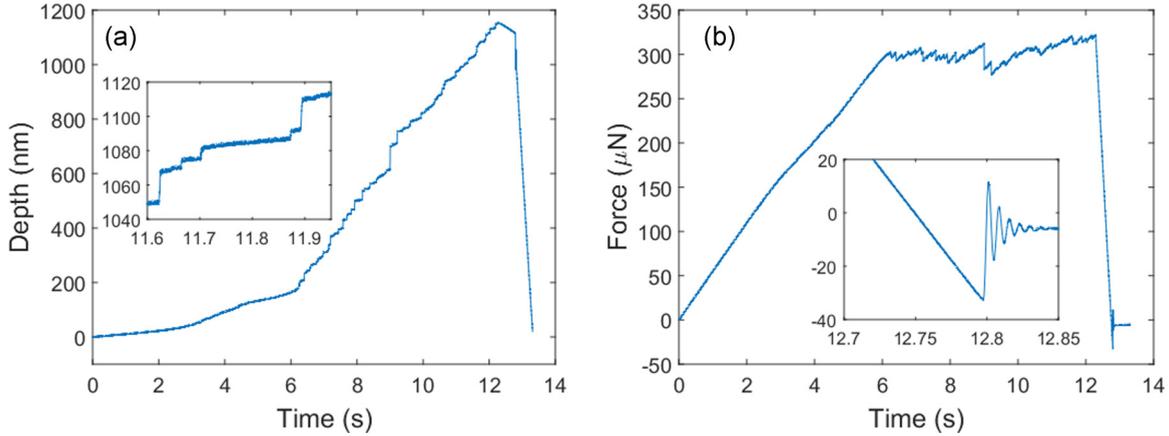
FIG. 1. (a) Full experimental depth vs time curve for one of the three Au specimens (the other two specimens are qualitatively similar). The vertical jumps in the curve are a macroscopic signature of slip avalanches, in which interacting dislocations collectively move (inset shows a magnification including several slip avalanches). (b) Full experimental force vs time curve for the same Au specimen. The inset of (b) shows the damped sinusoidal oscillation of the machine at the end of the unloading process.

applicable beyond mean-field theory to any avalanching system.

We further note that the external stress in a slip avalanche experiment is increased via either open-loop or closed-loop control; closed-loop control is facilitated by a proportional-integral-derivative (PID) controller that measures the actual strain rate and attempts to correct any deviations from the desired strain rate by adjusting the applied stress loading rate (this inherently-stress-controlled picture may be modified for inherently-strain-controlled devices). In a PID-controlled experiment, the experimenter specifies a desired set point for the stress or the strain as a function of time; the difference between the measured value and set point value is the "error" signal. The value of the directly experimentally controlled quantity (e.g., the voltage applied to an actuator) is then a sum of three terms: (1) a term proportional to the most recent value of the error signal, (2) a term proportional to the integral of the error signal, and (3) a term proportional to the derivative of the error signal. This simple picture may also be modified by adaptive-gain algorithms that tune the PID gains during an experiment. In an experiment without a PID controller, there is no such feedback loop, and the value of the experimentally controlled quantity instead follows a pre-defined trajectory without such "course correction" feedback. The analysis in this paper is done for open-loop experiments that do not include a PID controller, which is a distinctly different drive mode than the closed-loop PID-feedback mode used in Refs. [23,24].

II. IDENTIFYING THE MECHANICAL RESONANCE OF THE COUPLED MACHINE AND SPECIMEN

In this section, we analyze how a mechanical resonance affecting the applied force may naturally occur in certain types of nanoindentation experiments. The experimental data presented in this paper were obtained from three cylindrical Au ⟨001⟩ microcrystals of nominally 2-μm diameter and 6-μm height, prepared by annular focused ion beam milling from a bulk single crystal. The Au specimens were compressed using a flat punch tip in a Hysitron Triboindenter with a nominal

loading rate of 60 μN/s in open-loop force-controlled mode, and with a data acquisition rate of 16 kHz.

When the Au specimens are compressed, they undergo plastic deformation via slip avalanches, i.e., serrated flow. Slip avalanches occur in compressed crystals when interacting dislocations become unstable under the increasing compressive force and start to move, resulting in a sudden chain reaction in which moving dislocations in turn cause other dislocations to move [9]. Figure 1(a) shows the experimental depth vs time curve for one of the three Au specimens; slip avalanches are visible in this figure as nearly vertical segments of the curve. The same slip avalanches are also visible as sudden force drops in Fig. 1(b), which shows the force vs time curve for the same specimen.

When no compressed specimen is present, the nanoindentation system used in these experiments to impose uniaxial compression can be modeled as a damped harmonic oscillator; the indenter head is a "mass" that is suspended via an effective spring-and-damper [25,26]. In this experiment, we observe such oscillations of the unloaded machine near the end of the experiment [Figs. 1(b) and 2]. Fitting a damped sinusoid to this oscillation, $y(t) = A\sin(2\pi f(t - t_0))e^{-\tau(t-t_0)} + y_0$, yields parameters $f = 139/\text{s}$ and $\tau = 108/\text{s}$. These fitted parameters are consistent with observations of the same parameters in [26], in which $f = 136/\text{s}$ and $\tau = 118/\text{s}$. This earlier work also extracted the machine stiffness $k_{\text{machine}} = 319\,\text{N/m}$ by fitting a line to the force vs depth curve during an avalanche event [26]; using the above values other physical machine parameters were also derived [26]: $D_{\text{machine}} = 0.101\,\text{Ns/m}$, and $m_{\text{transducer}} = 0.429\,\text{g}$.

When a compressed specimen is present, as in the experiment reported here, the specimen itself can undergo both elastic and plastic deformation. We approximate the elastic deformation of the specimen as a second spring-and-damper pair [Fig. 3(a)]. When the transducer mass is displaced by any amount, the two springs are either extended or compressed by that same amount, so that the springs and dampers act in parallel on this indenter head mass and may be combined into a single spring-and-damper pair [Fig. 3(b)]. The equivalent spring constant and damping coefficient for motion
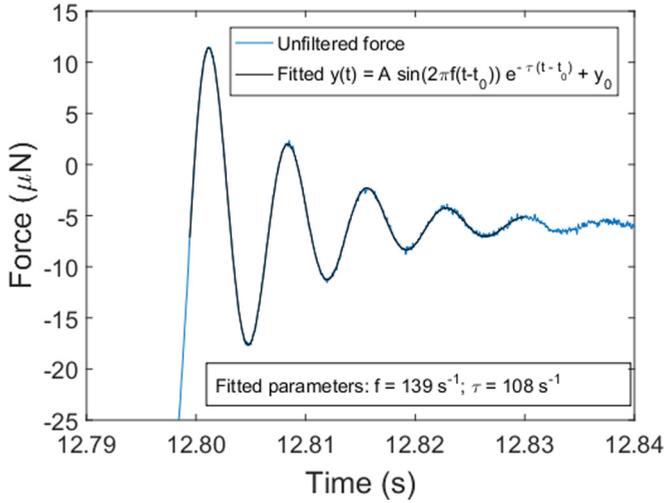
FIG. 2. Force vs time for the same Au specimen as in Fig. 1, magnified to highlight the oscillation of the unloaded nanoindenter. The fitted damped sinusoid is overlaid on the observed oscillation, with very good agreement between the experimental measurement and the fitted function, and also very good agreement between the fitted parameters and the parameters reported in Ref. [26].

of the transducer are therefore $k_{eq} = k_{machine} + k_{Au}$ and $D_{eq} = D_{machine} + D_{Au}$.

We estimate k_{Au} from the slope of the stress-strain curve during unloading. Since the unloading slope for each specimen appears to deviate from linearity when the specimen is more than 50% unloaded, we calculate the uncertainty in the fitted slope by progressively fitting a larger fraction of the unloading curve (from the first 20% of the unloading curve to the first 50% of the unloading curve) and report the maximum and minimum fitted slope as the uncertainty. To visually illustrate this linear fit, Fig. 4 shows the force vs depth curve for specimen 1, and the inset shows the linear fit to the first 50% of the unloading segment of the curve. The fitted unloading slope ranges are: $9.5e3\,\text{N/m} \leqslant k_{Au} \leqslant 1.0e4\,\text{N/m}$ (specimen 1); $9.7e3\,\text{N/m} \leqslant k_{Au} \leqslant 1.0e4\,\text{N/m}$ (specimen 2), and $1.0e4\,\text{N/m} \leqslant k_{Au} \leqslant 1.1e4\,\text{N/m}$ (specimen 3). In all three Au specimens, k_{eq} is dominated by k_{Au}, and k_{eq} may

(a)

FIG. 3. (a) Spring-damper model for the nanoindentation system used to compress the Au specimens. Note that for a given motion of the transducer mass, the springs add in a parallel configuration, not series. (b) Equivalent simplified spring-damper model for oscillations of the transducer mass.

FIG. 4. Force vs depth for the same Au specimen as in Figs. 1 and 2. The inset is a magnification of the unloading region; the linear fit to the first 50% of the unloading region is also shown.

be approximated as $1.0e4\,\text{N/m}$. We do not measure the value of the specimen damping coefficient D_{Au}, but this damping does not significantly shift the resonant period in this experiment. With this underdamped approximation, the resonant oscillation period of the machine under load should be near $2\pi/\omega_0 = 2\pi\sqrt{m/k_{eq}} = 1.3\,\text{ms}$.

This underdamped harmonic oscillator model may be verified by finding a peak in the power spectral density (PSD) of the velocity (the velocity is the derivative of depth) near frequency $1/(1.3\,\text{ms}) \sim 770\,\text{Hz}$. First, though, we investigate the PSD of the depth itself [27]. Figure 5(a) shows the unfiltered depth vs time of the plastic region of a single open-loop-tested Au specimen [this plastic region is a subset of the entire depth vs time trace shown in Fig. 1(a)], and Fig. 5(b) shows the PSD of the depth vs time in Fig. 5(a). Note that there is not a clear peak in the PSD of the depth at what we will show below is the experimentally determined resonant frequency of $\sim 750\,\text{Hz}$. The lack of a peak in the depth PSD is expected from the fact that avalanches are small background perturbations to the linear increase of depth vs time shown in Fig. 5(a). In order to observe the resonance peak in the PSD, it is important to view the PSD of the velocity instead of the PSD of the depth itself.

Figure 5(c) shows the velocity calculated via two-point differences of the unfiltered depth (see Appendix B), and Fig. 5(d) shows the PSD of this "unfiltered depth" velocity. In order to reduce the high-frequency noise, we applied a finite-impulse response (FIR) filter to the depth as described in [23]. Figure 5(e) shows the velocity calculated via two-point differences of the FIR-filtered depth, and Fig. 5(f) shows the PSD of this "filtered depth" velocity. Figure 5(e) shows that the FIR filter greatly enables avalanche detection by lowering the high-frequency noise floor (see Appendix A). The filtered and unfiltered velocity PSDs show a clear peak at the expected mechanical resonant frequency of $\sim 750\,\text{Hz}$, corresponding to the above-calculated period of roughly 1.3 ms; the agreement between these two values verifies the above damped-harmonic-oscillator model. We next investigate how
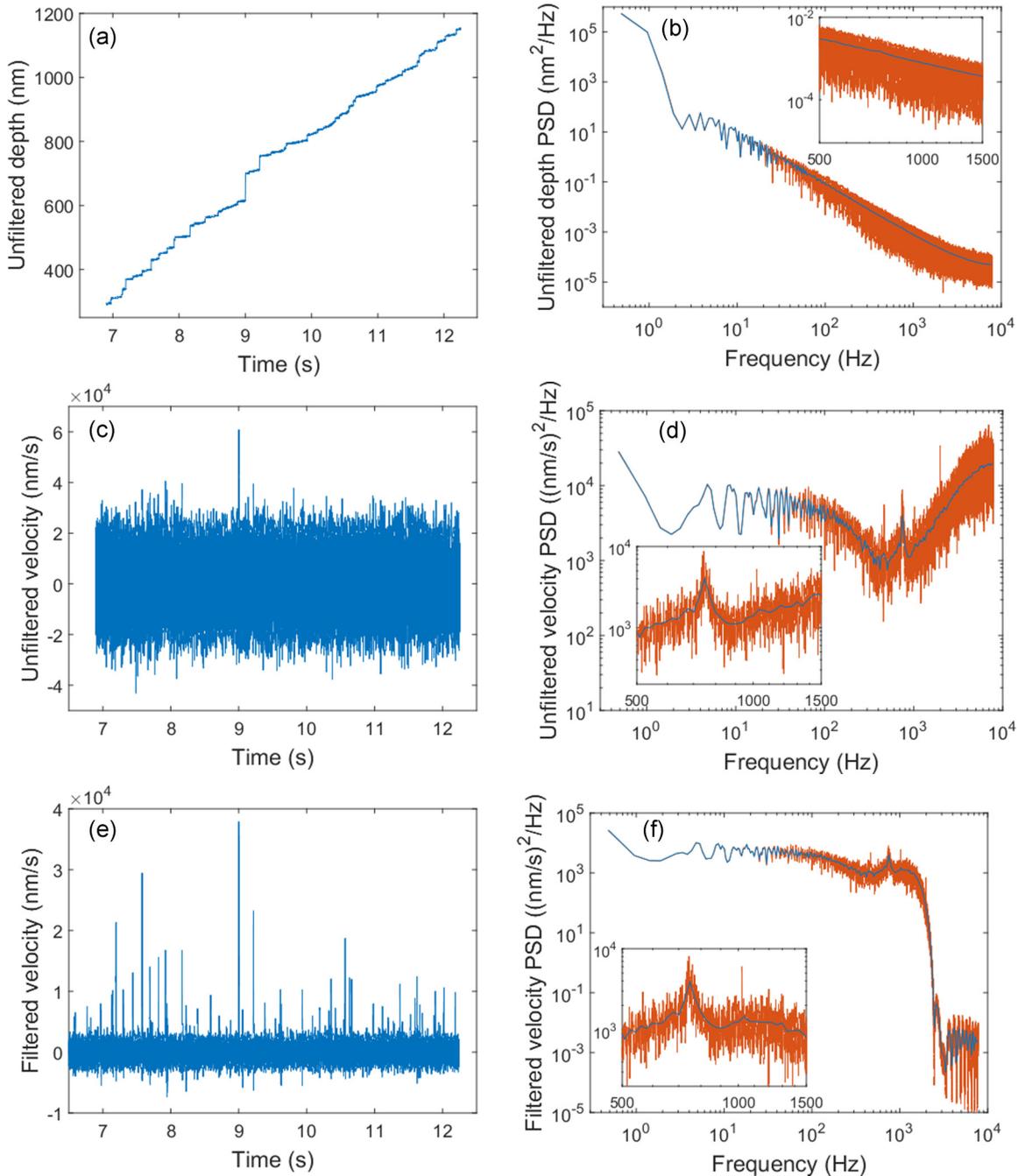
FIG. 5. (a) Plastic region of the unfiltered depth vs time for the same Au specimen as in Figs. 1, 2, and 4. (b) Power spectral density (PSD) of the unfiltered depth shown in (a). (c) Velocity vs time of the unfiltered depth, calculated via two-point difference. (d) PSD of the velocity shown in (c). Note the peak near ~750 Hz. (e) Velocity vs time of the filtered depth, calculated via two-point difference of the FIR-filtered depth. (f) PSD of the velocity shown in (e). All PSD curves (b), (d), and (f) are calculated via the Welch method [27] and are overlaid with a smoothed PSD curve. All PSD curves contain magnified insets spanning the mechanical resonant frequency of ~750 Hz.

the average slip-avalanche shapes are affected by these oscillations in this open-loop non-PID-controlled experiment.

III. AVALANCHE SHAPES IN EXPERIMENTS ON COMPRESSED Au ⟨001⟩

In this section we report experimental slip avalanche shapes in gold crystals, and we find signatures of the mechanical resonant frequency calculated above. These experimental

shapes agree well with the simulated shapes reported in Ref. [10], which are summarized in the subsequent section. In this experiment we use open-loop force control in order to isolate and detect the effect of machine oscillations on avalanche dynamics.

Each individual slip avalanche has a "shape," which is the velocity as a function of time while the avalanche is occurring [i.e., the derivatives of the upward jumps visible in Fig. 1(a)]. Each avalanche also has a "size," which is

defined as the total distance the depth increases during the avalanche (or equivalently, as the integral of the shape of the avalanche). A set of avalanches may be partitioned into groups of avalanches of similar size, and an average avalanche shape may be calculated for each of these size-defined groups.

Prior experiments have shown that slip avalanche sizes in Au $\langle 001 \rangle$ can be described by a mean-field model with a quasistatic boundary [18,19]. However, if oscillations occur on the same timescale as the avalanche durations, then fitting a power-law distribution to the avalanche sizes may not yield an accurate fit to check the predicted power-law exponents [10]. Therefore, for the experiments reported in this paper, we do not rely on fitting power-law exponents to assess the validity of any specific avalanching model for these experiments. Instead, our aim is to report the average avalanche shapes and compare them to the average shape predicted by this mean-field model as motivated by the above-mentioned prior experiments. Although individual avalanche shapes may be quite jerky and sharp, the average avalanche shape in the monotonic mean-field model is a smooth function of time: $f(t) = A\, t\, e^{-Bt^2}$, where A and B depend on the avalanche size [15]. Therefore, in addition to computing the average experimental avalanche shapes, we also examine whether the monotonic mean-field average shape matches the experimentally observed average shapes.

Figure 6 shows the experimental size-binned average avalanche shapes. As the figures progress from Figs. 6(a) and then to 6(b)–6(e), larger size-binned average avalanche shapes are included with the smaller size-binned shapes from the previous figures. Each black curve shows the monotonic mean-field shape function scaled to match the largest avalanche shape in each subfigure. In addition, each red curve shows a modified shape function (again scaled to the largest avalanche in each subfigure) that decays with an alternative exponent: $A\, t\, e^{-Bt}$, where the exponent is proportional to t (as an alternative to the above mean-field shape, in which the exponent is proportional to t^2). This modified shape function was selected since it was used previously [23] to represent the avalanche shape albeit without considering potential effects of applied force oscillations. We neither assert that this modified shape function represents true material response nor that it is the most accurate function to fit the shapes; we use it here only to highlight deviations from the mean-field predictions.

The series of subfigures in Fig. 6 shows the evolution of these experimental average shapes from approximating the usual average shape at small avalanche sizes [Figs. 6(a) and 6(b)], to deviating from this shape at medium avalanche sizes [Fig. 6(c)], and again to closely approximating this shape at larger avalanche sizes [Figs. 6(d) and 6(e)]. Note that in the mean-field model, the avalanche duration increases with avalanche size according to a power law with an exponent of $1/2$ [15].

The midsize (akin to mid-duration) average avalanche shapes [Figs. 6(b), 6(c), and 6(d)] do not closely follow the usual average avalanche shape $f(t) = A\, t\, e^{-Bt^2}$. Instead, there are visible distortions in these avalanche shapes, which have durations near the period of the damped sinusoid derived above ($\sim$1.3 ms). The differences between the usual shape and the midsize shape are consistent with the timescale of oscillations in the applied force. However, the largest-size average avalanche shape [Fig. 6(e)] closely follows the monotonic-driving average shape. Figure 6 thus suggests that when the oscillation period of the coupled nanoindenter-plus-compressed-specimen is comparable to the avalanche duration, the oscillations influence the avalanche dynamics causing the avalanches to deviate from the expected mean-field shape.

The above-calculated oscillation period matches the observed distortions in the avalanche shapes, indicating that this damped-harmonic-oscillation mode is active during slip avalanches. Since the compression experiment can be modeled by the damped harmonic oscillator shown in Figs. 3(a) and 3(b), the excitation of this mechanical resonance in turn oscillates the force applied to the Au specimen via the machine spring, thereby affecting the ongoing stress-dependent avalanche dynamics.

IV. SIMULATED AVALANCHES WITH EXTERNAL OSCILLATIONS

In order to illustrate how the above experimentally observed shapes are consistent with oscillations in the external force, we present simulated shapes from the same model as in Ref. [10]. We use different model parameter values than those in Ref. [10] in order to show that observing oscillatory features in the simulated shapes do not rely on fine-tuning model parameters.

We model avalanching systems as a collection of coupled weak spots, or "cells." When the stress on a cell exceeds a threshold failure stress that cell slips forward a finite distance, and this forward motion increases the stress on all of the other cells. This stress increase may cause more cells to fail, which may in turn cause even more cells to fail. These chain reaction dynamics lead to avalanches as described in detail previously [14,22,28].

The avalanching system is modeled as N cells (here $N = 10^5$), each of which is at position u_i and experiences stress τ_i ($1 \leqslant i \leqslant N$). The cells are elastically coupled to each other through the positive mean-field elastic interaction J/N, and to a boundary spring of stiffness K_L. One end of this boundary spring is assumed to be externally controlled with position u_0, and the other end is coupled to the average position of each cell in the avalanching system. The resulting stress on each cell is

$$\tau_i = \frac{J}{N-1} \sum_j (u_j - u_i) + K_L(u_0 - u_i).$$

In most previous studies of this model, the external force transmitted by the boundary spring increases linearly at an adiabatically slow rate. This boundary condition is enforced by increasing the position u_0 of the experimentally controlled end of the spring as a linear function of time, so that $u_0 = vt$. Instead, in order to include oscillations of the boundary-applied force, we take the externally-controlled end of the spring to be an underdamped sine wave that starts at the beginning of each avalanche: $u_0 = Z\, e^{-t/\theta} \sin(\omega t)$ [10]. The simulation units cannot directly be mapped to physical units; instead we work with units such that $J = 1$, and we include a weak loading spring $K_L = 1 - 1/\sqrt{N}$. In these units,
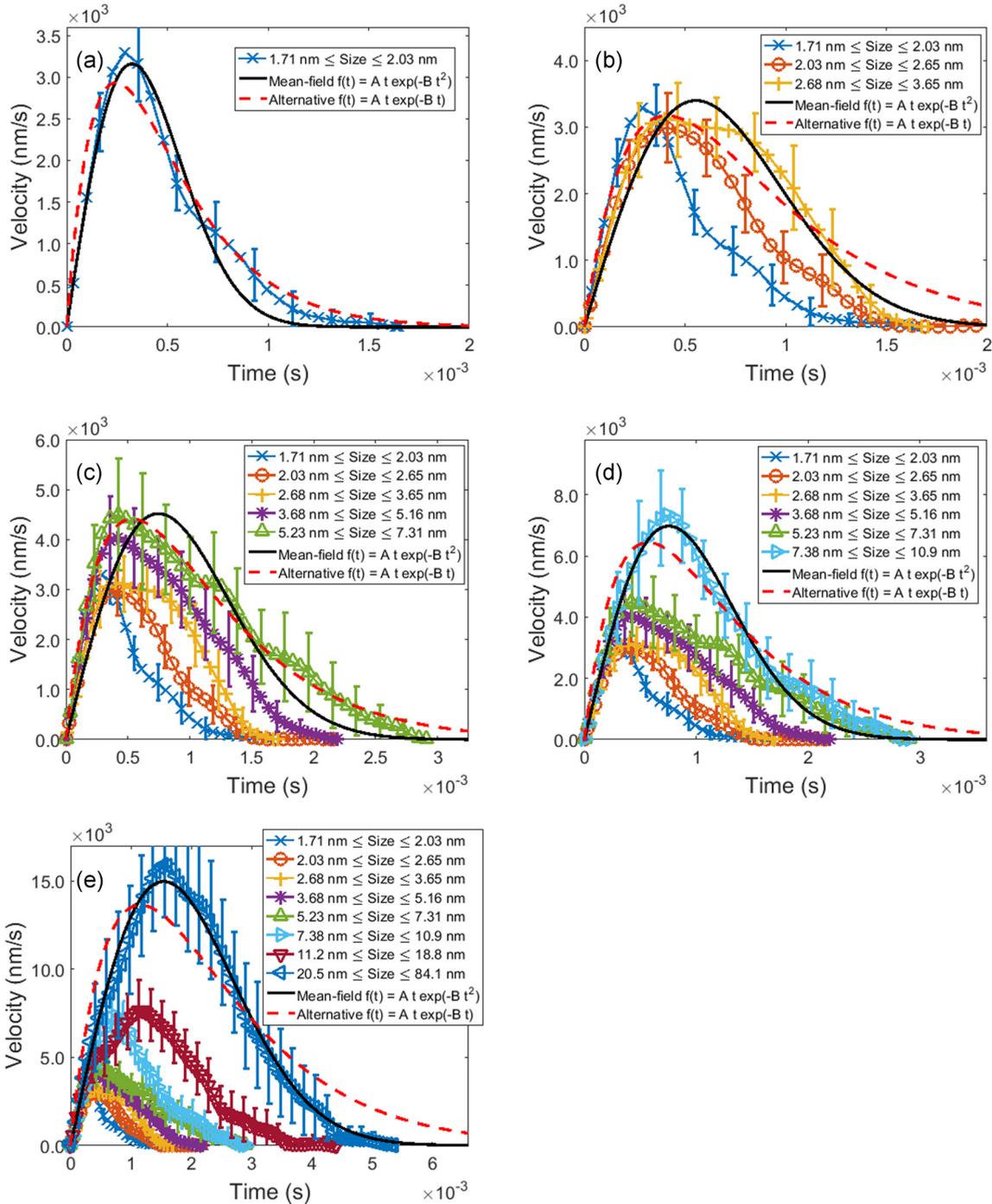
FIG. 6. Average avalanche shapes for slip avalanches in Au crystals. Avalanches have been binned together by avalanche size, and the average avalanche shape in each size-bin is shown. (a) (top left) shows the average shape for avalanches in the smallest size-bin. Averages in larger bins are shown progressively in (b)–(e). Each black curve shows the predicted mean-field shape function scaled to match the largest avalanche in the figure, and the red curve represents an alternative shape function, again for comparison with the largest avalanche in the figure. Note the distortions that are similar to the distortions of the simulation with oscillation (Fig. 7), which are consistent with the machine oscillation timescale. Error bars are drawn at every third point to avoid clutter. The five smallest shapes are each an average of 35 events, while the three largest shapes are all an average of 28 events.

the simulated oscillation amplitude $Z = 15/(N\,K_L)$. We also discretize time into equal time steps Δt (so that $\Delta t = 1$, $\omega = 2\pi/50$, and $\theta = \omega/10$).

We define the "size" of an avalanche in this model to be the total number of cells that fail during an avalanche, and the "shape" of an avalanche in this model to be the number of cells that fail at each simulated time step of the avalanche. Figure 7 shows the simulated average avalanche shapes in a format similar to Fig. 6. To summarize key points:

(1) Figure 7(a) shows the average simulated shape for the smallest-size bin. The average simulated shape shows good agreement with the monotonic mean-field shape. This
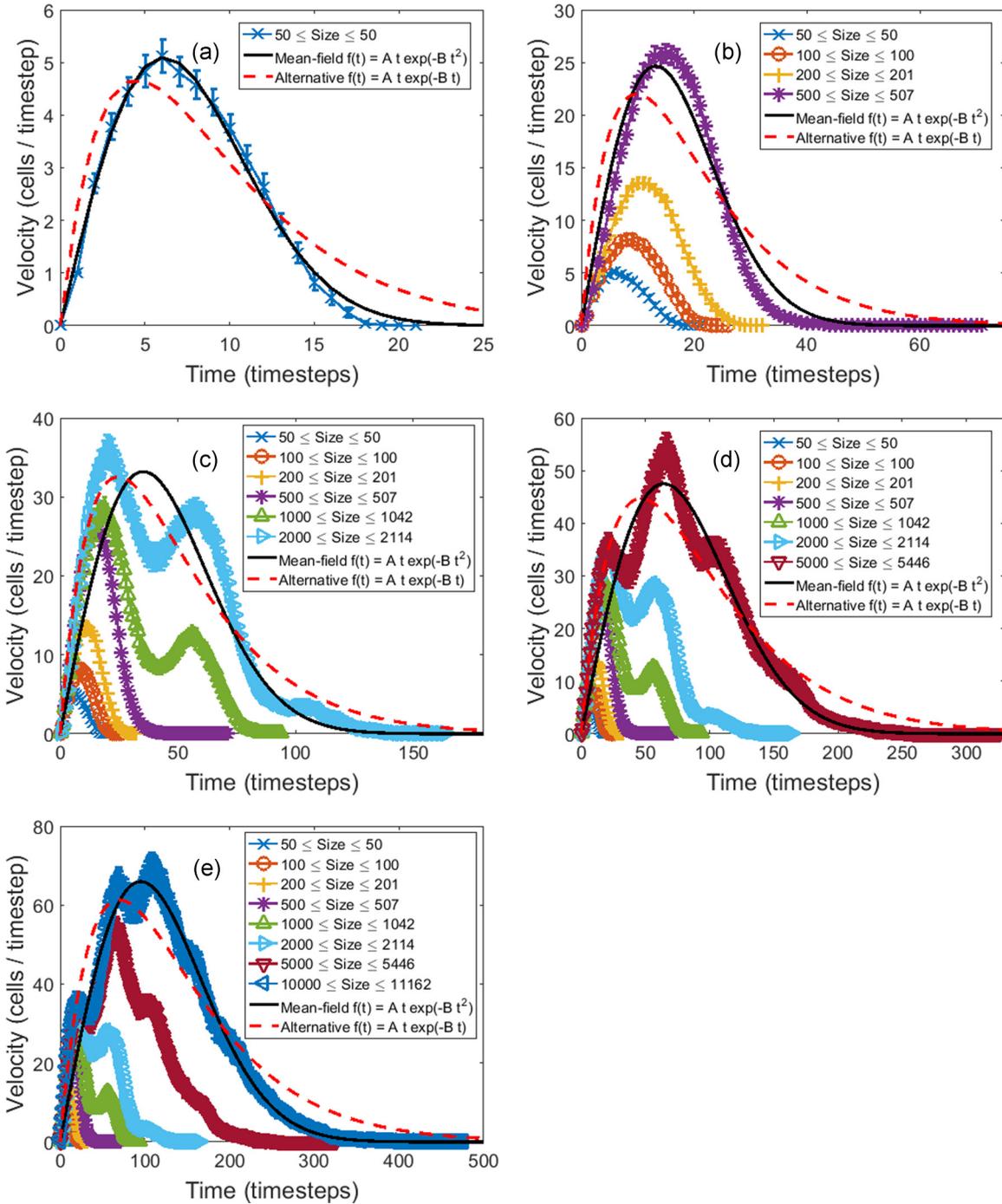
FIG. 7. Average simulated avalanche shapes generated by the mean-field model of avalanche dynamics with a damped-oscillating external force instead of a linearly increasing external force, presented similarly to Fig. 6. Each black curve shows the predicted monotonic mean-field shape function scaled to match the largest avalanche shape in the figure, and the red curve represents an alternative shape function, again for comparison with the largest avalanche in the figure. Each plotted shape is the average of 250 avalanche events. The intermediate-size shape [Fig. 7(c)] shows better agreement with the alternative reference shape. Almost all error bars in this figure are smaller than the marker size. Note that with the simulations, we are able to generate a very large range of avalanche size values (three orders of magnitude), wider than the range achievable with physical experiments.

agreement is expected, because most avalanches in this bin have durations shorter than the oscillation period.

(2) Figure 7(e) shows the average simulated shapes up to the largest-size bin. Similar to the largest-size experimental avalanche shape [Fig. 6(e)], the largest-size simulated

avalanche shape [Fig. 7(e)] again matches the shape for monotonic driving.

(3) The largest average simulated shapes in Figs. 7(c) and 7(d) deviate from the monotonic-driving shape, as shown by the quasiperiodic "ledges" and "bumps" distorting the shapes.

In this paper and in Ref. [10] we analyzed the effects of external oscillations in simulated avalanche shapes by using a specific model (the mean-field model of Refs. [14,22,28]). However, we emphasize (1) that we expect similarly distorted avalanche shapes may be obtained by introducing an oscillating boundary to other non-mean-field models, and (2) that this paper does *not* claim that the similarity between the distorted shapes in the experiments and mean-field model is proof of the validity of the mean-field model to these experimental results. The mean-field model is being used here not to prove its validity, but rather to provide a framework for thinking about how oscillations affect a general class of avalanching models. Of the variety of avalanching models, we chose the mean-field model's predicted avalanche shape for comparison to the experimental Au ⟨001⟩ results because previous papers have indicated agreement between Au ⟨001⟩ avalanche statistics and mean-field predictions [18,19].

The results of applying an oscillatory boundary to the mean-field model are intended to help conceptualize how the experimental results are consistent with a generic avalanching model that has an oscillatory external force. Indeed, the external oscillation may be thought of as "competing" with the quasistatic dynamics typically assumed. The avalanche dynamics of the mean-field model may be described probabilistically: at each time step of an avalanche, the number of cells that fail during that time step, n_t, may be thought of as being drawn from a Poisson distribution with $\lambda = n_{t-1}$ [28]. In this way, if many cells fail during one time step of an avalanche, then it is likely that many cells will fail during the subsequent time step also. This stochastic process "competes" with the extra cells that fail or do not fail due to the difference of the oscillating external force between one time step and the next time step. If the avalanche happens to grow very large, with a series of time steps in which very many cells fail, then the small perturbation of the n_t values may not make an observable difference to the usual monotonic avalanche dynamics. Therefore, consistent with the results in this paper, the large-avalanche average shapes agree with the monotonic shape.

In contrast, for avalanches of an intermediate size, the competition between those two processes may not heavily favor the standard monotonic dynamics. In that case, the external oscillation may be observed in the avalanche shapes if the avalanche durations are long enough to include a full oscillation period of the external force.

We wish to emphasize two things about this qualitative mental picture. First, as mentioned before, it is difficult if not impossible to measure the actual quantitative values of these two competing scales in an actual physical slip avalanche experiment; delving further into the quantitative details of this mental picture would not be experimentally useful [10]. Second, this way of thinking about the model does not rely on specifically mean-field dynamics; for example, this analysis of competing scales can also be generalized to avalanching models other than the above-described Poisson-distribution dynamics. The above discussion of how oscillations affect avalanche dynamics is useful not just for mean-field dynamics but rather for a wider class of avalanching models, of which each may be interpreted in their own way [29–31].

Given the agreement between the oscillation frequency derived in Sec. II and the timescale of the distortions in the experimental shapes, and given the agreement between the experimental shapes and the simulated shapes, we conclude that machine oscillations can interact with the avalanche dynamics via the oscillatory applied stress. Fortunately, the fact that this resonance depends on the effective spring constant of the specimen provides a way to avoid this effect in experiments, since the specimen spring constant depends on the specimen dimensions. This mechanical oscillation can be tuned by changing the cross-sectional area or the height of the specimen, and therefore this effect can be mitigated by choosing suitable specimen dimensions, or by choosing a different avalanching material that yields avalanche durations on a different timescale than the coupled oscillation period. Finally, it is interesting to note that in future experiments the specimen dimensions can be tuned to deliberately introduce oscillations thereby possibly providing a mechanism to test the effects of dynamic triggering on the avalanche dynamics.

V. CONCLUSION

These experiments and simulations show that oscillations in the average avalanche shapes may diagnose oscillations in the applied force on the avalanching system. These results also show that the observable effects of these oscillations may be diminished by adjusting the experimental parameters; for example, changing the cross-sectional area or the height of a compressed microcrystal will change the specimen stiffness and therefore change the oscillation frequency.

In both the simulations and the experiments, the average avalanche shapes in the largest-size bin follow the usual mean-field shape for monotonic driving. The durations of the avalanches averaged together in these largest bins are much longer than the characteristic oscillation period of the applied stress. Similarly, the average shapes in the smallest-size bin also follow the usual mean-field shape because the durations of most of the avalanches averaged together in these smallest bins are shorter than the characteristic oscillation frequency of the applied stress. The average shapes in the intermediate-size bins, however, show deviations from the monotonic mean-field shape that are the manifestation of the oscillations. This result suggests that applied-force oscillations do not equally affect avalanche dynamics for avalanches of different sizes.

Even if an avalanching system includes applied-force oscillations, the resulting avalanche dynamics may still be indistinguishable from the dynamics of a system with an adiabatically slow linearly increasing force if the timescales of the avalanche durations and the external oscillation are sufficiently different. This type of timescale mismatch may be why such applied-force oscillations have not been observed in avalanche dynamics in other experimental systems. In contrast, in the experiments discussed here, the oscillation period in some cases was comparable to or even shorter than the avalanche duration thereby producing artifacts in the observed avalanche shapes. If the goal of an experiment is to interpret materials behavior in light of avalanche dynamics, the specimen dimensions must be chosen to ensure that the avalanches and oscillations do not influence each other.

APPENDIX A: EFFECTS OF FILTERING

When working with inherently noisy data to analyze temporal features of the data, it is critical to recognize the tradeoffs between maintaining the fidelity of temporal features and smoothing the signal to eliminate noise [32]. For the experimental data in this work, the velocities of the individual avalanches were calculated by taking the two-point difference of adjacent depth values after smoothing the depth curve with a FIR filter with a cutoff frequency of 1.6 kHz. To demonstrate the effects of temporal distortion of features through data smoothing, we also used a velocity calculation involving further smoothing after the FIR filter is applied (Fig. 8). This alternative calculation applies the MATLAB movingslope() function to the FIR-filtered depth-time data; this
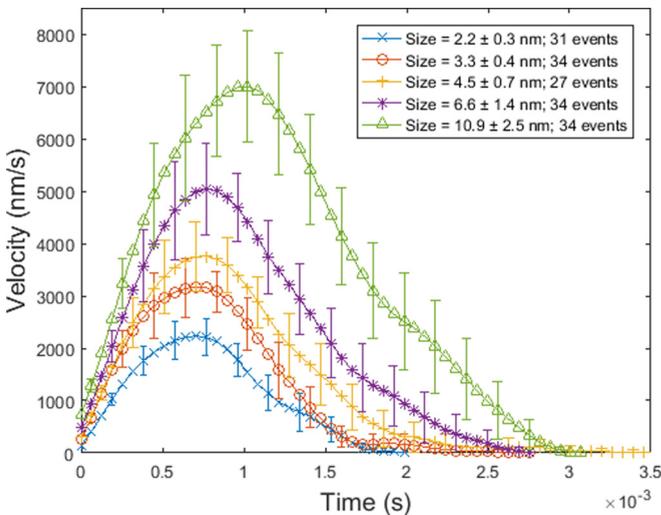
FIG. 8. Average avalanche shapes for slip avalanches in Au crystals from experiments, analyzed with an alternative shapes-extraction method. This alternative method first uses the same FIR filter as used in Fig. 6, but then further smooths the velocity by applying a least-squares linear fit across multiple experimental data points. This extra smoothing introduces a tradeoff: as extra smoothing is applied, the experimental noise is reduced even further, but the avalanche oscillations become smoothed out and are less visible to the point that they may not be properly recognized as oscillations.

function calculates a least-squares linear fit spanning multiple data points at each experimental observation time instead of taking just a two-point difference [33]. The number of data points in the least-squares fit is dynamically calculated for each avalanche and ranges between 2 and 9 data points; further detail about this calculation is included in Ref. [23].

We find that when we apply this more extensive smoothing to the open-loop data investigated here, the oscillations in the average avalanche shapes become too smoothed out to see (Fig. 8). Clearly then there is a tradeoff between (1) applying further filtering, which may reduce the noise, versus (2) not applying further filtering, which may enable visual observation of the oscillations in the average avalanche shapes. Smoothing is sometimes applied in order to highlight the macroscopic trends of a stress-strain curve; however if one wants to view whether oscillations are present in the avalanche dynamics, then not applying further smoothing will help keep the oscillations visible. In the present work, the smoothing that was performed was minimized to prevent temporal distortions of the avalanche shapes.

APPENDIX B: AVALANCHE DETECTION ALGORITHM

The beginning of each avalanche is identified as when the increasing velocity crosses 0 nm/s, and the end of each avalanche is defined as when the decreasing velocity crosses 0 nm/s. In order to prevent noise fluctuations from being detected as avalanches, we keep only the avalanches with total sizes exceeding a minimum threshold (1.6 nm for these experiments).

Resonant oscillations are sometimes observed to occur immediately after an avalanche ends in these experiments, and these events may mistakenly be detected as avalanches. We therefore use a modified but still automated method of extracting slip avalanches in these experiments. We first detect all avalanches with size greater than 1.6 nm. We then impose a "lockout" time: any avalanches with start times occurring within 2 ms of the end of the previous avalanche are discarded. This means that if there is a resonant "ringing" oscillation after a large avalanche ends, with several consecutive up-trends of the depth vs time spuriously being detected as avalanches because they exceed the 1.6 nm threshold, then each such up-trend will serve to lock out the next up-trend until there is a window of time with no detected events >1.6 nm. In this way, the up-trend portions of post-avalanche ringing are prevented from being spuriously detected as avalanche events.

However, we also observe that some avalanches have precursor avalanches that occur immediately before them. To ensure that the above-mentioned "lockout time" does not discard these actual nonspurious avalanches, we modify the above algorithm so that any avalanche with size greater than 6 nm is automatically kept and is not discarded by the lockout-time algorithm. Qualitatively, we find that this automated algorithm does a good job of selecting the avalanches that we would have selected when subjectively inspecting the curve "by eye" while avoiding most of the spurious-ringing events.

[1] M. Bretz, R. Zaretzki, S. B. Field, N. Mitarai, and F. Nori, Europhys. Lett. **74**, 1116 (2006).

[2] D. V. Denisov, K. A. Lörincz, J. T. Uhl, K. A. Dahmen, and P. Schall, Nat. Commun. **7**, 10641 (2016).

[3] D. M. Dimiduk, C. Woodward, R. LeSar, and M. D. Uchic, Science **312**, 1188 (2006).

[4] M.-C. Miguel, A. Vespignani, S. Zapperi, J. Weiss, and J.-R. Grasso, Nature (London) **410**, 667 (2001).

[5] D. Schorlemmer, S. Wiemer, and M. Wyss, J. Geophys. Res. **109**, B12307 (2004).

[6] M. Zaiser, J. Schwerdtfeger, A. S. Schneider, C. P. Frick, B. G. Clark, P. A. Gruber, and E. Arzt, Philos. Mag. **88**, 3861 (2010).

[7] R. Maass and P. M. Derlet, Acta Mater. **143**, 338 (2018).

[8] W. J. Wright, Y. Liu, X. J. Gu, K. D. Van Ness, S. L. Robare, X. Liu, J. Antonaglia, M. LeBlanc, J. T. Uhl, T. C. Hufnagel, and K. A. Dahmen, J. Appl. Phys. **119**, 084908 (2016).

[9] M. Zaiser, Adv. Phys. **55**, 185 (2007).

[10] L. W. McFaul, W. J. Wright, J. Sickle, and K. A. Dahmen, Mater. Res. Lett. **7**, 496 (2019).

[11] L. W. McFaul, Ph.D. thesis, University of Illinois at Urbana-Champaign, 2019.

[12] J. Gomberg, P. A. Reasenberg, P. Bodin, and R. A. Harris, Nature (London) **411**, 462 (2001).

[13] P. A. Johnson and X. Jia, Nature (London) **437**, 871 (2005).

[14] K. A. Dahmen, Y. Ben-Zion, and J. T. Uhl, Phys. Rev. Lett. **102**, 175501 (2009).

[15] D. S. Fisher, Phys. Rep. **301**, 113 (1998).

[16] J. Antonaglia, W. J. Wright, X. J. Gu, R. R. Byer, T. C. Hufnagel, M. LeBlanc, J. T. Uhl, and K. A. Dahmen, Phys. Rev. Lett. **112**, 155501 (2014).

[17] D. V. Denisov, K. A. Lörincz, W. J. Wright, T. C. Hufnagel, A. Nawano, X. J. Gu, J. T. Uhl, K. A. Dahmen, and P. Schall, Sci. Rep. **7**, 43376 (2017).

[18] N. Friedman, A. T. Jennings, G. Tsekenis, J.-Y. Kim, M. Tao, J. T. Uhl, J. R. Greer, and K. A. Dahmen, Phys. Rev. Lett. **109**, 095507 (2012).

[19] R. Maass, M. Wraith, J. T. Uhl, J. R. Greer, and K. A. Dahmen, Phys. Rev. E **91**, 042403 (2015).

[20] J. T. Uhl, S. Pathak, D. Schorlemmer, X. Liu, R. Swindeman, B. A. W. Brinkman, M. LeBlanc, G. Tsekenis, N. Friedman, R. Behringer, D. Denisov, P. Schall, X. J. Gu, W. J. Wright, T. Hufnagel, A. Jennings, J. R. Greer, P. K. Liaw, T. Becker, G. Dresen, and K. A. Dahmen, Sci. Rep. **5**, 16493 (2015).

[21] Y. Cui, G. Po, and N. Ghoniem, Phys. Rev. Lett. **117**, 155502 (2016).

[22] K. Dahmen, D. Ertas, and Y. Ben-Zion, Phys. Rev. E **58**, 1494 (1998).

[23] G. Sparks and R. Maass, Acta Mater. **152**, 86 (2018).

[24] G. Sparks and R. Maass, Eur. Phys. J. B **92**, 15 (2019).

[25] J. Hay, P. Agee, and E. Herbert, Exp. Tech. **34**, 86 (2010).

[26] G. Sparks, P. S. Phani, U. Hangen, and R. Maass, Acta Mater. **122**, 109 (2017).

[27] P. D. Welch, IEEE Trans. Audio Electroacoust. **15**, 70 (1967).

[28] M. LeBlanc, Ph.D. thesis, University of Illinois at Urbana-Champaign, 2016.

[29] M. Ovaska, A. Lehtinen, M. J. Alava, L. Laurson, and S. Zapperi, Phys. Rev. Lett. **119**, 265501 (2017).

[30] P. D. Ispánovity, L. Laurson, M. Zaiser, I. Groma, S. Zapperi, and M. J. Alava, Phys. Rev. Lett. **112**, 235501 (2014).

[31] J. Lin and M. Wyart, Phys. Rev. X **6**, 011005 (2016).

[32] M. LeBlanc, A. Nawano, W. J. Wright, X. J. Gu, J. T. Uhl, and K. A. Dahmen, Phys. Rev. E **94**, 052135 (2016).

[33] J. D'Errico, Movingslope, https://www.mathworks.com/matlabcentral/fileexchange/16997-movingslope, 2007.